



The Effect of Milling Time and Speed on Solid Solubility, Grain Size, and Hardness of Al-V Alloys

C.S. Witharamage, J. Christudasjustus, and R.K. Gupta

Submitted: 5 October 2020 / Revised: 9 February 2021 / Accepted: 28 February 2021 / Published online: 24 March 2021

The effect of milling time and speed on solid solubility of V in Al and grain refinement was studied. High-energy ball milling was used to produce Al-xV ($x = 2, 5$, and 10 at.%) alloys at milling speeds of 280 and 350 RPM. The ball-milling time was varied from 10 to 100 hours. The ball-milled alloys were consolidated under uniaxial pressure of 3 GPa at room temperature. The solid solubility of V and grain size after ball milling of Al-xV alloys were estimated using the x-ray diffraction (XRD) analysis. High-energy ball milling imparted the nanocrystalline structure and formation of Al-V solid solution. Grain refinement and solid solubility of V in Al were dependent on the milling speed, milling time, and V content in the alloy.

Keywords grain refinement, high-energy ball milling, nanocrystalline aluminum alloys, solid solubility

1. Introduction

Recent demand regarding increasing the fuel efficiency of vehicles via reducing the weight and decreasing material consumption via increasing the service life led to research on developing new alloys owning an excellent strength-to-weight ratio without compromising the corrosion resistance (Ref 1–6). Aluminum alloys are widely used in the aerospace, marine, and automotive industries due to the high strength-to-weight ratio (Ref 7–10). However, commercial alloys produced by conventional processing techniques show a compromise between mechanical and corrosion properties, which limits their use in several applications. Mechanical and corrosion properties of aluminum alloys can be controlled by choosing appropriate composition and processing routes. Several non-conventional alloy production techniques such as high-pressure torsion (Ref 11, 12), sputter deposition (Ref 13–19), ion implantation (Ref 13, 20–23), and high-energy ball milling (Ref 2, 6, 24, 25) have been demonstrated to cause significant enhancement of the properties in Al alloys. Our previous work has shown the possibility of producing Al alloys with high strength and corrosion resistance by high-energy ball milling (HEBM) (Ref 1–3, 25). For example, Gupta et al. produced Al-Cr alloy using HEBM, which resulted in nanocrystalline structure, uniform dispersion of fine intermetallic phases, and the extension of the solid solution of Cr in Al which caused a significant enhancement in both corrosion and mechanical properties (Ref 26). The main advantages of HEBM are the ability to refine grain size below 100 nm and producing microstructure far from the equilibrium. For example, Esquivel et al. have

shown the solubility of V in the ball-milled powder of Al-5 at.%V to be ~ 3 at.% which is $\sim 10^6$ times higher than the solid solubility of V in Al at room temperature in equilibrium state (Ref 3, 27). Such a high solid solubility of the alloying elements resulted in high strength and corrosion resistance in the HEBM Al alloys.

HEBM is a complex process where the powder particles undergo severe plastic deformation, repetitive fracture, and cold welding during HEBM (Ref 28, 29). The defects and dislocations density increase with continuous milling that leads to grain refinement, rapid inter-diffusion of the elements being milled, and the formation of a solid solution. Kinetics and extent of grain refinement and formation of the solid solution depend on numerous parameters including type of ball mill, milling speed, milling time, temperature, size of balls, hardness and density of the milling media, and the ball-to-powder ratio (Ref 6, 28–30). Among these parameters, optimization of milling time is significant for bulk production in a shorter time. The effect of ball milling time on the microstructural evolution has been reported in several studies (Ref 31–35). However, the literature on the formation of the solid solution of Al with corrosion-resistant alloying elements is scarce (Ref 32, 37). It has been reported that milling of Al with corrosion-resistant alloying at 280 RPM for 100 hours caused the formation and supersaturated solution. (Ref 2, 3, 25, 27). 100 hours is a long milling time, and therefore, optimizing milling time is of great merit. This work presents the optimization of the milling time to achieve high solid solubility and grain refinement. Solute (V) content was varied from 2 to 10 at.%, and milling was performed at 280 and 350 RPM to determine the effect of milling time on the grain size and solubility of V in Al. V was used in this study due to its effectiveness in increasing corrosion resistance, hardness, and thermal stability (Ref 2, 3, 27, 36).

2. Experimental

2.1 Alloy Synthesis and Consolidation

Al-xV ($x = 2, 5$, and 10 at.%) alloy powders were produced using Fritsch P-5/4 planetary ball mill starting with Aluminum

C.S. Witharamage, J. Christudasjustus, and R.K. Gupta,
Department of Materials Science and Engineering, North Carolina State University, Raleigh, NC 27695; and Department of Chemical, Biomolecular, and Corrosion Engineering, The University of Akron, Akron, OH 44325. Contact e-mail: rkgupta2@ncsu.edu.

powder with 99.7% purity (mesh size of $-50/+100$) and Vanadium powder with 99.8% purity (mesh size of 325). Both Aluminum and Vanadium powder were weighted inside a glove box with a high purity Argon environment (Oxygen <25 ppm) to maintain inert atmospheric conditions and eliminate oxidation of powders during milling. The weighted powder was loaded into hardened stainless-steel jars with stainless steel balls of 10 mm diameter. The ball-to-powder weight ratio was kept 16:1. 1.5 wt.% of the total powder weight of stearic acid was added into each jar as a process controlling agent. High-energy ball milling was performed at 280 and 350 RPM separately. The 30 min of pause was kept after each hour of milling. Alloy powders that recovered from ball milling were cold compacted using the auto pellet press with the tungsten carbide die under the uniaxial pressure of 3 GPa. The load was gradually increased in 16 steps until reaching a final pressure of 3 GPa and held for 15 minutes.

2.2 Characterization

The Rigaku SmartLab x-ray diffractometer was employed to perform x-ray diffraction (XRD) with filtered Cu K α radiation ($\lambda = 0.15406$ nm). The XRD test was used to identify the formation of intermetallic, unalloyed elements, calculate the extension of solid solubility of V, and calculate average grain size. The XRD analysis was performed in the 20 range of 15° – 85° with step size 0.02° and scanning rate 1° per min. The solid solubility was calculated using the major peak in the scanning associated with the (111) plane. The average grain size was estimated using Scherrer's formula (Ref 2, 37–40) after eliminating instrumental broadening. The procedure for the calculation of grain size and solid solubility is described elsewhere (Ref 2, 37–42).

The scanning electron microscopy (SEM) was performed for the powder samples and bulk sample separately using Tescan Lyra 3 FIB-FESEM at 20 kV accelerating voltage with a working distance of 10 mm. The polishing up to $0.05\text{ }\mu\text{m}$, followed by ultrasonic vibrational cleaning in ethanol, was done for the bulk sample to perform the SEM characterization. The SEM images of Al-xV ($x = 2, 5$ and 10 at.%) at 280 and 350 RPM for the time interval of 10, 20, 40, 60, and 100 hours from powder samples were taken to observe the change in the size and structure of the particles with the increase in the V content. In bulk samples, the back-scattered electron (BSE) images of Al-xV ($x = 2, 5$, and 10 at.%) at 280 and 350 RPM

for the time interval of 10, and 100 hours were taken to understand the microstructure.

2.3 Hardness

Wilson Tukon 1202 hardness tester was employed to estimate the Vicker hardness of the samples. 50 g of the load was applied to the sample, and the dwelling time of the indenter was 10 s. At least 10 indentations were applied, with a separating distance of approximately 6 times the length of a single indentation to calculate the average hardness.

2.4 Potentiodynamic Polarization Test

The test specimens of Al-xV (2.5 and 10 at.%) were mounted in epoxy and grounded 1200 grit SiC paper finish followed ultrasonic cleaning. The sample edges were coated by epoxy resin (Araldite) and allowed for curing for around 12 hours. A conventional three-electrode electrochemical cell was used, with a platinum mesh as a counter electrode and saturated calomel electrode (SCE) as the reference electrode. A Biologic VMP-300 potentiostat under the control of EC-lab software was used for the electrochemical tests. The samples were immersed in 0.01 M NaCl solution for 30 minutes for the stabilization, and anodic polarization was performed starting from 50 mV below the open circuit potential (OCP) with the scanning rate of 0.167 mV/s toward the active direction until reached the $200\text{ }\mu\text{A/cm}^2$ current density. Then, the scanning direction was reversed. These experiments were repeated at least three times to assure reproducibility.

3. Results and Discussion

3.1 Scanning Electron Microscope (SEM)

Figure 1, 2, 3, 4, 5 and 6 shows the backscattered electron (BSE) images for Al-x at.%V alloy powder samples produced by HEBM for 10 to 100 hours at a milling speed of 280 and 350 RPM. Fine flake type morphology was observed for Al-2 at.%V after 10 hours of ball milling at 280 RPM (Fig. 1a). The flakes were replaced by the particles after 20 hours or milling (Fig. 1b). The size of these particles reduced till 40 hours of milling followed by agglomeration with the increase in ball milling time till 100 hours (Fig. 1c). The milling speed had a

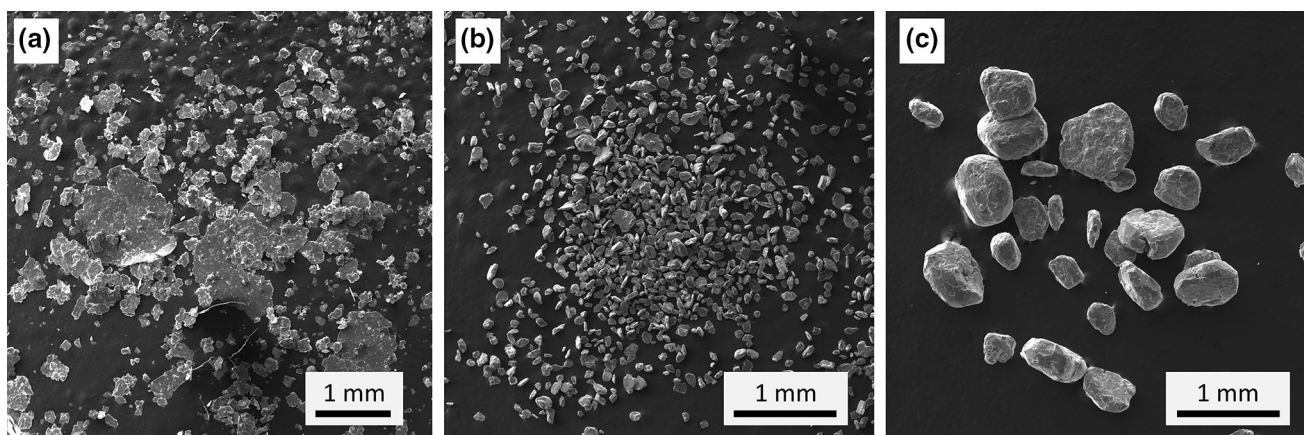


Fig. 1. BSE images of Al-2 at.%V alloy after HEBM at 280 rpm for: (a) 10, (b) 20, and (c) 100 hours

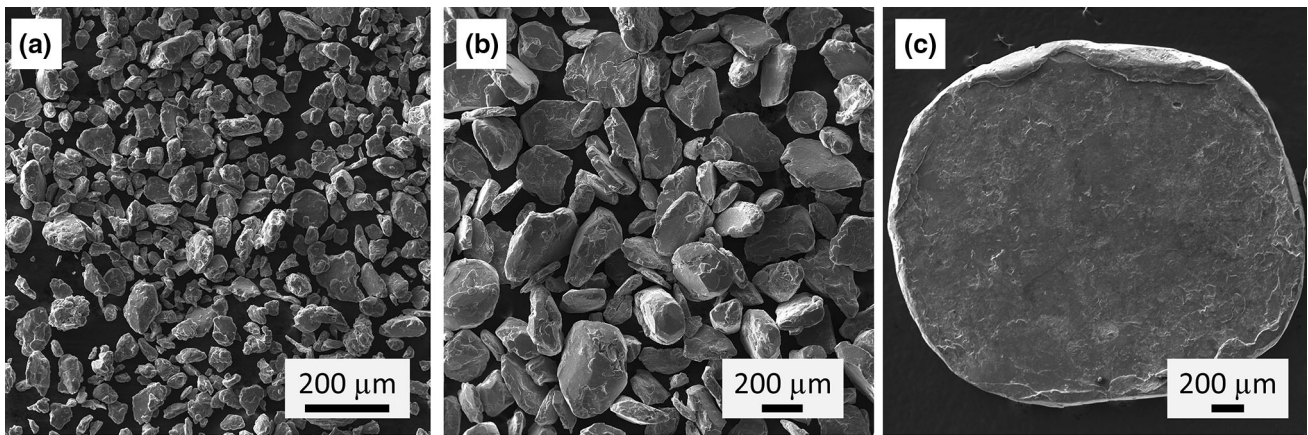


Fig. 2. BSE images of Al-2at.%V alloys after HEBM at 350 rpm for: (a) 10, (b) 40 and (c) 100 hours

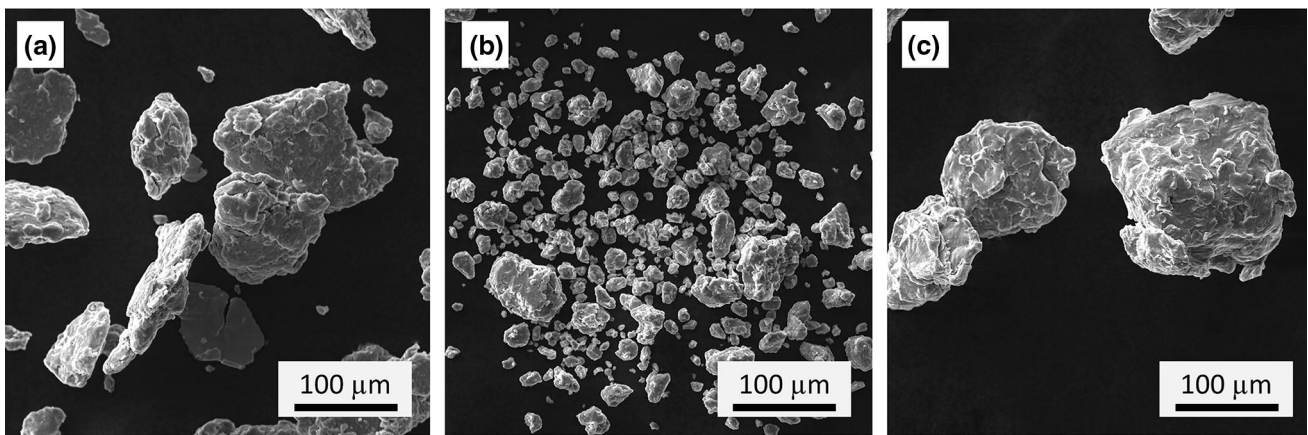


Fig. 3. BSE images of Al-5at.%V alloy after HEBM at 280 rpm for: (a) 10, (b) 20 and (c) 100 hours

noticeable influence on the morphology of the powder. The milling of Al-2at.%V at 350 rpm does not lead the flake formation after 10 hours (Fig. 2a) of milling, and particle size increment was observed up to 40 hours of milling (Fig. 2b) followed by agglomeration of particles with further milling. Fully consolidated, disk type pellets were produced after 100 hours of ball milling at 350 RPM (Fig. 2c). The diameter of the disks varied from 1 to 5 mm, and thickness was typically \sim 500 micron. These discs can be used to study the structure and properties of ball-milled alloys. The formation disc after 100 hours of milling is an example of in situ consolidation which is reported to occur in special conditions for specific metals and alloys. Mechanisms of in situ consolidation during HEBM is not well understood. Production of in situ consolidated alloys has been reported for Cu (Ref 43, 44), Al-Cr (Ref 26), Fe-Cr-Ni (Ref 45) alloys.

The evolution of the particle morphology was impacted by the V content in the alloys. The formation of the flakes was not observed for Al-5at.%V and Al-10at.%V alloys (Fig. 3, 4, 5 and 6) for both milling speeds. For milling at 280 rpm, both Al-5at.%V and Al-10at.%V alloys (Fig. 3 and 5, respectively) showed a decrease in the particle size till 40 hours (Fig. 3b and 5b) and then began to coarsen with the milling time and formed coarse particles after 100 hours of milling (Fig. 3c and 5c).

Whereas, in 350 RPM significant particle size reduction appeared after 10 hours of milling in Al-5at.%V and Al-10at.%V (Fig. 4a and 6a, respectively) and further milling lead to coarsening of the particles (Fig. 4b and 6b). For both the milling speeds, the average particle sizes after a given milling time reduced with the increase in V content.

High energy ball milling time is one of the main key parameters which directly influence the distribution and morphology of the milled powders. The correlation between milling time and the specific area of the powder can be expressed using the following equation (Ref 46).

$$\ln \frac{A_m - A_0}{A_m - A} = kt \quad (\text{Eq 1})$$

According to Eq 1, long hours of milling can refine the powders. But continuous crushing for an infinite time is not possible due to the deterioration of powder properties. For example, cold welding would reduce the amount of powder that can be recovered after the milling. Besides, milling for a long time would cause contamination from the milling media and decomposition of the extended solid solution to the thermodynamically stable phases (Ref 47, 48). Hence, it is crucial to examine the effect of ball milling time to achieve a favorable composition with desired properties.

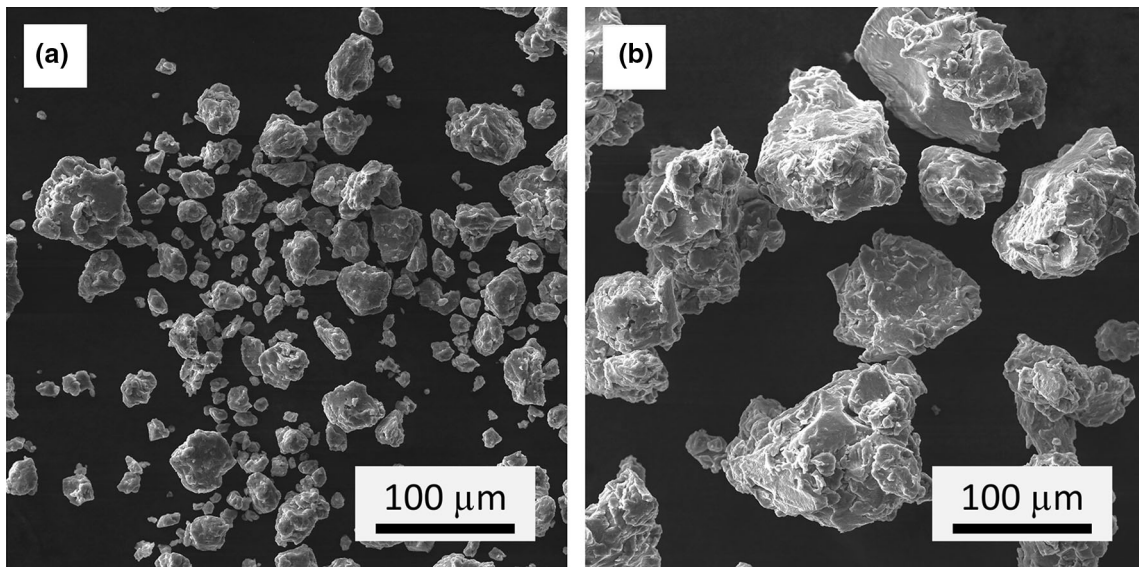


Fig. 4. BSE images of Al-5at.%V alloy after HEBM at 350 rpm for: (a) 10, and (b) 100 hours

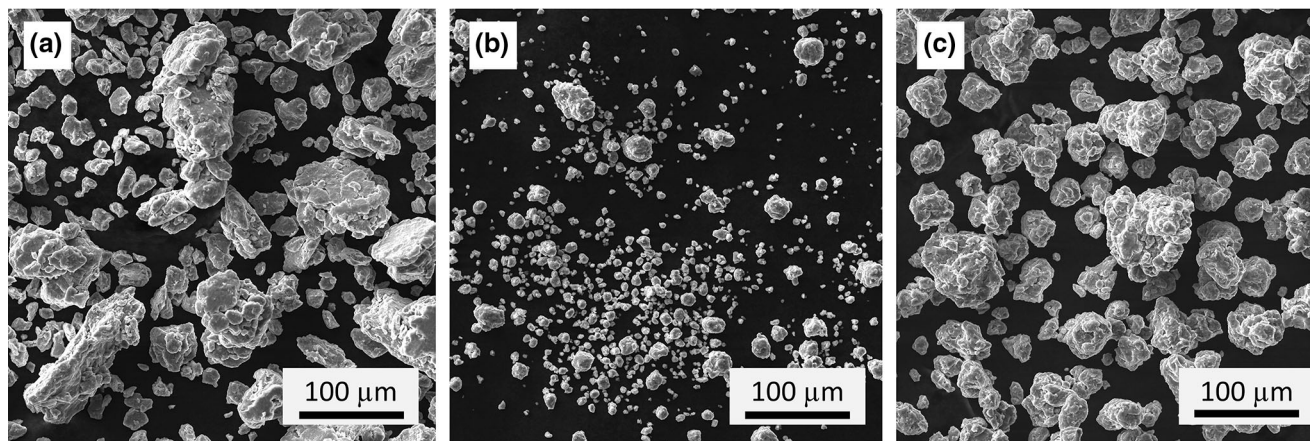


Fig. 5. BSE images of Al-10at.%V alloy after HEBM at 280 rpm for: (a) 10, (b) 20 and (c) 100 hours

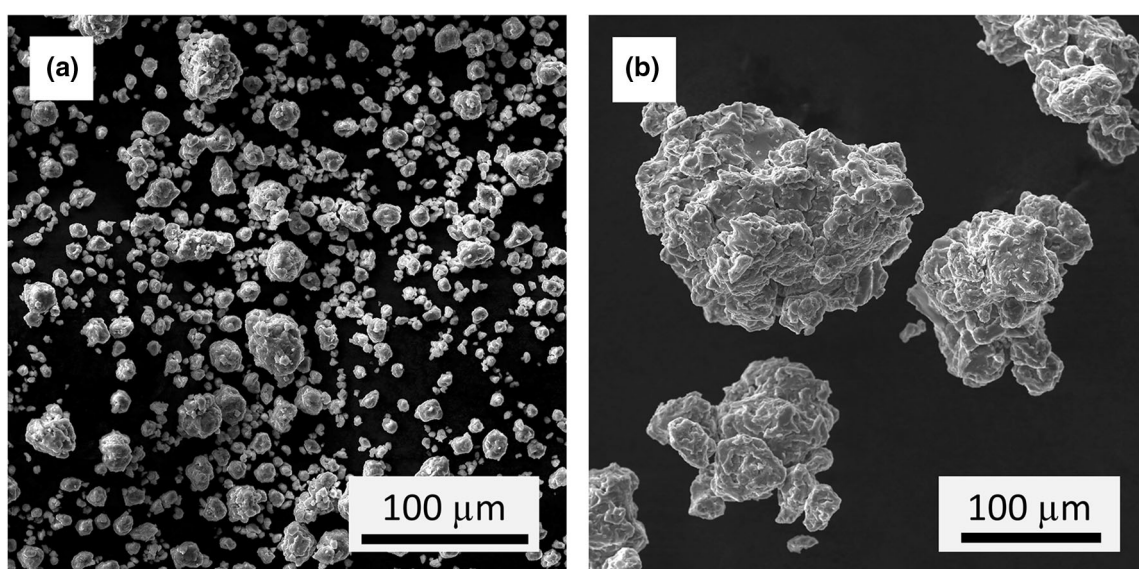


Fig. 6. BSE images of Al-10at.%V alloy after HEBM at 350 rpm for: (a) 10, and (b) 100 hours milling times

3.2 X-ray Diffraction (XRD) Analysis

X-ray diffraction analysis for the Al-x at.%V alloys produced by HEBM at 280 and 350 RPM for various milling times is shown in Fig. 7, 8, 9, 10, 11 and 12. A zoomed-in region for FCC Al (111) peak was shown to elucidate the peak shift and change in peak intensity and broadening with the milling time and speed. The Al-2at.%V (Fig. 7a) showed only Al peaks after milling at 280 RPM for milling up to 100 hours, which indicated that either no Al-V phase was formed, or the volume fraction of the Al-V phase was little to be detected by XRD. XRD peaks corresponding to Al_3V were observed after milling Al-2at.%V at 350 RPM for 100 hours, which indicated the formation of Al_3V by the decomposition of supersaturated solid solution which formed during milling up to 60 hours. Increase in the temperature during milling may be attributed to the decomposition of the solid solution.

Peaks corresponding to V, confirming the presence of unalloyed V, were appeared in Al-5at.%V and Al-10at.%V after milling at 280 RPM for 10 hours, which disappeared during further milling, indicating either incorporation of V in solid solution or formation of Al-V phases. V peak after milling at 350 RPM for 10 hours was not observed which indicated that ball milling at 350 RPM facilitated the incorporation of Vanadium into the solid solution or the formation of intermetallics at the early stage of milling. In Al-10at.%V, a peak corresponding to Al_3V (Ref 3) was observed after milling from 20 to 60 hours and then disappeared after 100 hours of milling. Such evolution of the phases during HEBM is not very well understood and needs further work focused on studying the alloying and phase transformation during HEBM. Nevertheless, information about the formation of various phases is useful in selecting the right processing parameters in producing alloys via HEBM.

The zoomed-in regions of XRD spectra as presented in Fig. 7b, 8, 9, 10, 11 and 12b clearly show peak shifts toward the right (higher 2θ values), which indicates a decrease in the lattice parameters caused by the solid solubility of V in Al. The peak shift would increase with increasing V solubility. Ball milling of Al-2at.%V (Fig. 7b) at 280 rpm showed a continuous

peak shift toward higher 2θ values with increase in milling time from 10 to 100 hours. For Al-5at.%V and Al-10at.%V alloys, the peak shifted toward higher 2θ values until 40 hours of milling at 280 RPM (Fig. 9b, 10 and 11b, respectively), denoting the increment of solid solubility. After milling at 60 hours, the peak began to shift toward a lower 2θ value indicating the loss of V from a solid solution (Fig. 9b, 10 and 11b). HEBM of Al-2at.%V at 350 RPM (Fig. 8(b)) showed the peak shift toward higher 2θ values until 40 hours of milling indicating the highest solid solubility and then gradually decreased with the appearance of Al_3V at 100 hours of milling. The decrease in peak shift after reaching a maximum value indicates a reduction in solid solubility and formation of intermetallic. The intermetallic would form due to the decomposition of the supersaturated solid solution to the thermodynamically stable phases: Al and Al_3V . In Al-5at.%V at 350 RPM (Fig. 10b), there is no significant peak shift in either direction. Similarly, in Al-10at.%V at 350 RPM (Fig. 12b), a significant peak shift toward the lower 2θ values was observed due to the formation of the Al_3V intermetallic phase that caused the loss of V atom from the solid solution.

The solid solubility of V in Al, determined by XRD analysis, is presented with the ball milling time for both 280 and 350 RPM (Fig. 13a and b). Ball milling time required to achieve the highest solid solubility was dependent upon both composition and milling speed. For 280 RPM, Al-2at.%V achieved the highest solid solubility (1.99at.%) in 100 h, whereas Al-5at.%V and Al-10at.%V required 40 hours of milling. For 350 RPM Al-2at.%V, Al-5at.%V, and Al-10at.%V required 40, 10, and 10 hours, respectively, to achieve the highest solid solubility (Fig. 13a and b). The highest achievable solid solubility at 350 RPM was lower compared to that at 280 rpm for all the compositions, which indicates that high milling speed does not necessarily result in the higher solubility. At 350 rpm, the higher impact energy due to the high milling speed caused the formation of the solid solution and the grain refinement at the early stage of milling. Nevertheless, observed reduction in the solid solubility over the milling time in Al-5at.%V, and Al-10at.%V at 350 rpm may be attributed to the

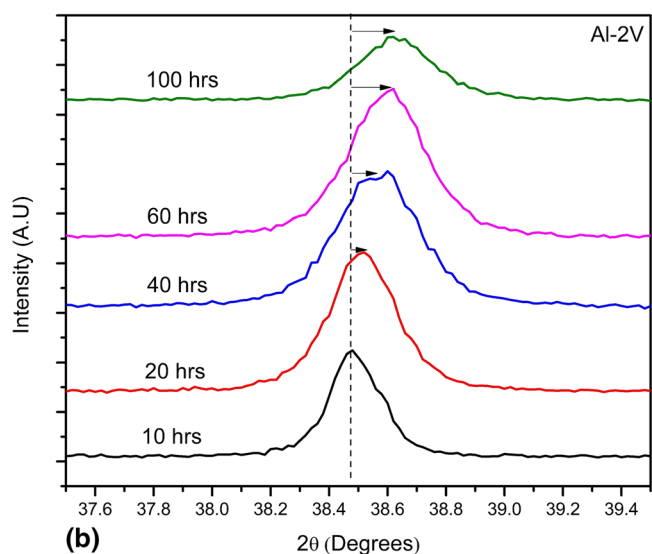
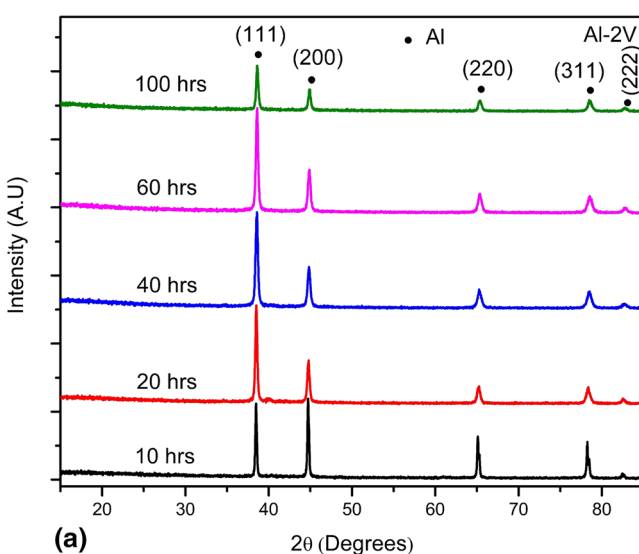


Fig. 7. XRD scans for HEBM Al-2at.%V for different milling times (a) complete XRD scan at 350 RPM, (b) zoomed region at 280 RPM, showing peak shift corresponding to Al (111) for various milling times

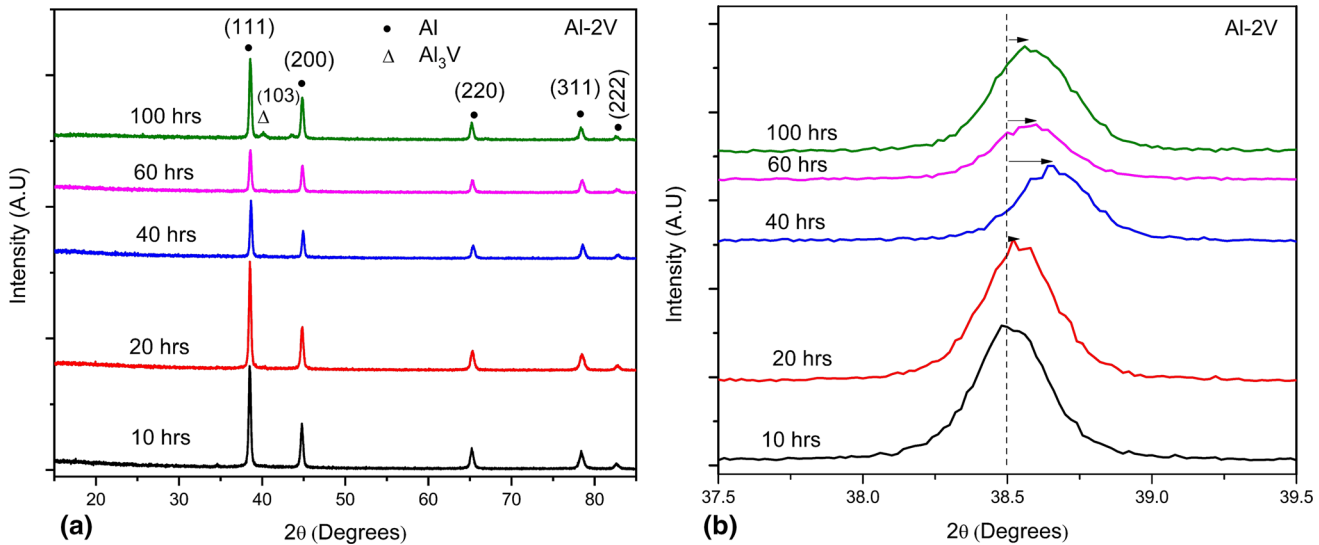


Fig. 8. XRD scans for HEBM Al-2at.%V for different milling times (a) complete XRD scan at 350 RPM, (b) zoomed region at 350 RPM, showing peak shift corresponding to Al (111) for various milling times

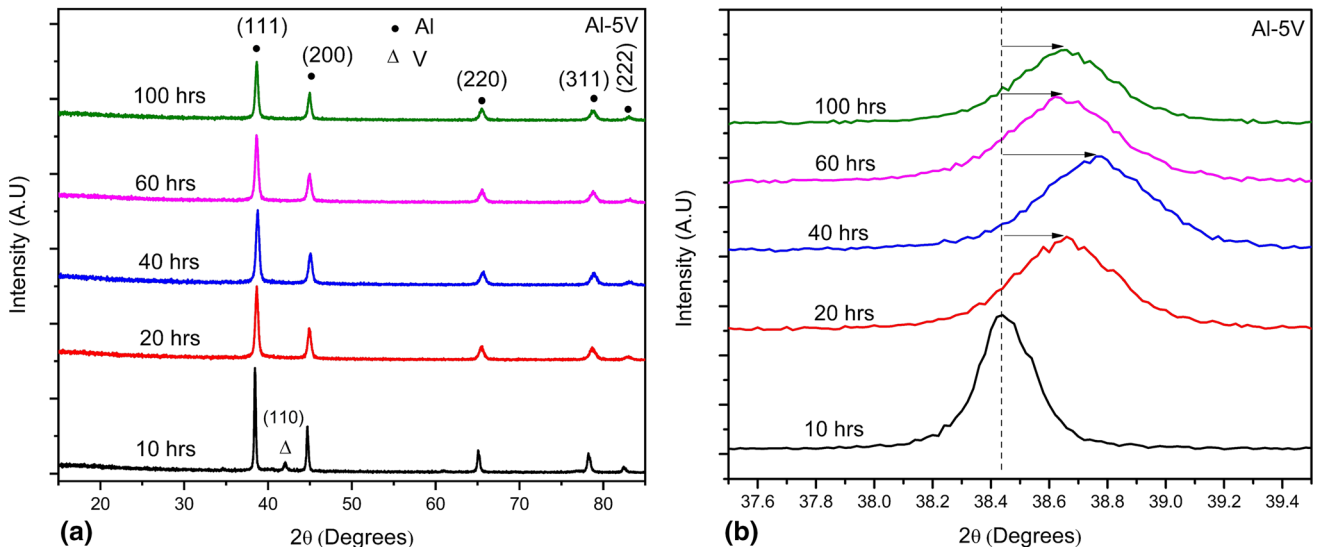


Fig. 9. XRD scans for HEBM Al-5at.%V for different milling times (a) complete XRD scan at 280 RPM, (b) zoomed region at 280 RPM, showing peak shift corresponding to Al (111) for various milling times

decomposition of the solid solution due to increase in temperature with the continuous milling (Ref 58).

Observations from the XRD were supported by the SEM and EDX analysis. BSE images of the HEBM cold compacted Al-xV ($x=2, 5$ and 10 at.%) after 10 and 100 hours of milling at 280 and 350 RPM are shown in Fig. 14, 15 and 16. In Al-2at.%V after 10 hours of milling at 280 RPM (Fig. 14(a)), layer type morphology was observed due to poor bonding between flack type powder particles during cold compaction. Similarly, the other two compositions at 280 RPM (Fig. 15a and 16a) also showed an inhomogeneous microstructure after 10 hours of ball milling, which reflects that insufficient milling time leads to inhomogeneous microstructure with unalloyed V particles. While all three compositions after 10 hours of ball milling at 350 RPM (Fig. 14c, 15 and 16c) showed a well-distributed homogeneous microstructure without unalloyed V particles,

indicating that higher RPM would facilitate homogeneous microstructure at the early stage of milling. Neither unalloyed V particles nor coarse intermetallics were observed in all the cases after 100 hours of milling which indicated that HEBM was able to cause a homogeneous distribution of V in the Al matrix. However, the amount of porosity has increased dramatically with the increment of V content for both speeds. Also, extremely fine ($\sim 1 \mu\text{m}$) bright particles were observed in high magnifications. EDXS analysis was performed on these particles and confirmed that Fe and Cr rich phase conjugate to the abrasion of milling media. Characteristics of the matrix and secondary phases play a crucial role in determining the corrosion performance (Ref 26, 49-51). Due to the absence of coarse intermetallics and unalloyed V in the microstructure, suitable alloying content may enhance the corrosion resistance of Al-xV ($x = 2, 5$ and 10 at%) alloys.

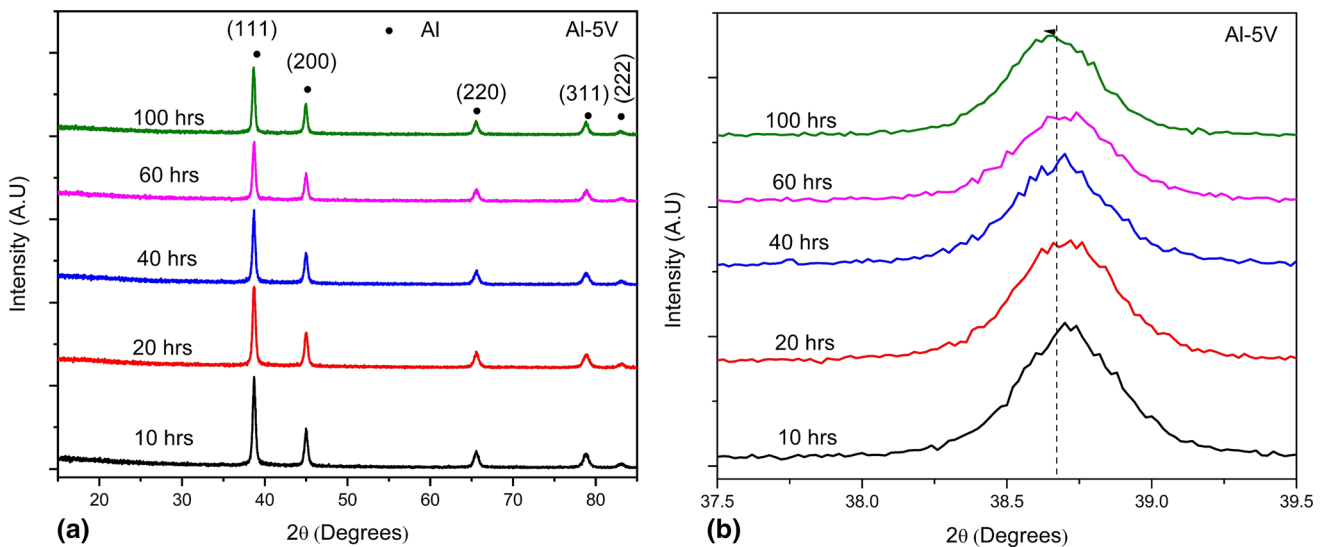


Fig. 10. XRD scans for HEBM Al-5at.%V for different milling times (a) complete XRD scan at 350 RPM, (b) zoomed region at 350 RPM, showing peak shift corresponding to Al (111) for various milling times

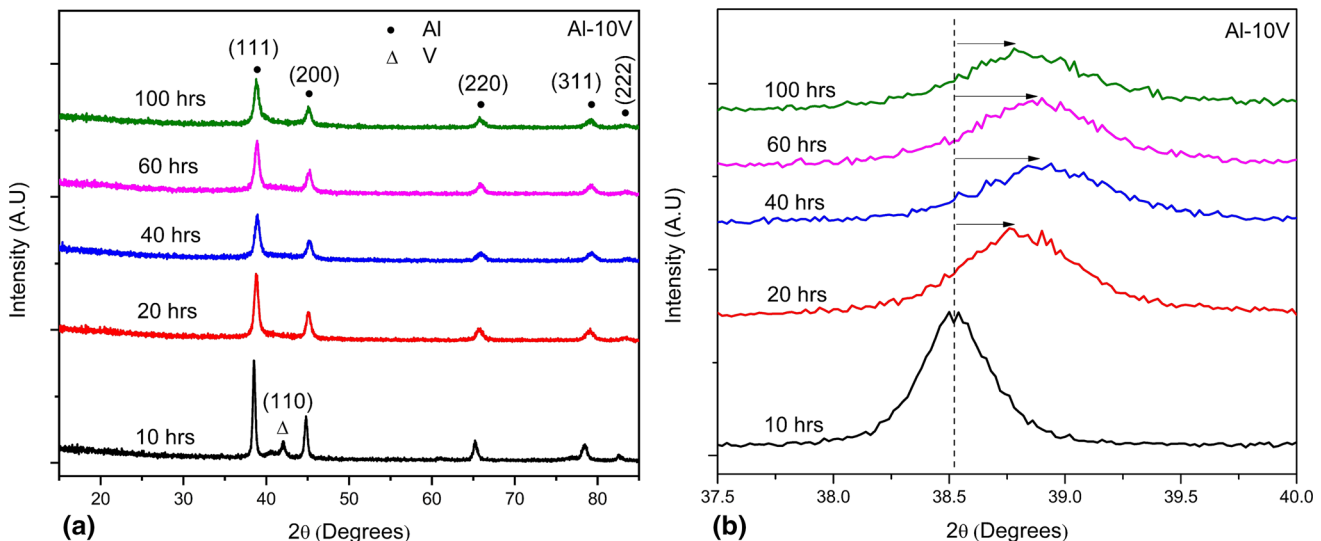


Fig. 11. XRD scans for HEBM Al-10at.%V for different milling times (a) complete XRD scan at 280 RPM, (b) zoomed region at 280 RPM, showing peak shift corresponding to Al (111) for various milling times

The grain size variation with the ball milling time for each composition was calculated and presented as shown in Fig. 17a and b. The average grain size for all compositions was <100 nm confirming the formation of a nanocrystalline structure. The grain size decreased with the increment of ball-milling time and amount of Vanadium, which is in agreement with the reported literature about the enhancement of grain refinement with the increment of solute content and milling time (Ref 3, 50, 52). Enhanced grain refinement due to addition of solute has been attributed to increased work hardening and decreased dynamic recovery during milling (Ref 50, 52). The first 40 hours of ball milling at 280 RPM showed a rapid grain size reduction followed by an insignificant fluctuation. Whereas at 350 RPM, grain refinement is already achieved within the first 10 hours of ball milling, and no significant change in grain size with increasing milling time. This observation supports the reported

literature that higher rpm would facilitate rapid grain refinement at the early stage of milling (Ref 28, 29, 52).

3.3 Vickers Microhardness

Figure 18a and b show the average Vickers microhardness variation with the milling time for both 280 and 350 RPM, respectively. During the first 40 hours of milling at 280 RPM, hardness increased rapidly, followed by sluggish change with further ball milling. Change in hardness can be observed that significant grain refinement and solid solubility increment in the first 40 h of ball milling followed by insignificant change with continuous ball milling which is in good agreement with hardness fluctuation at 280 RPM.

At 350 RPM, the influence of the milling time on the hardness was dependent upon the composition. Al-2at.%V did not show a significant change in hardness with ball milling time. Whereas Al-5at.%V showed a significant improvement of

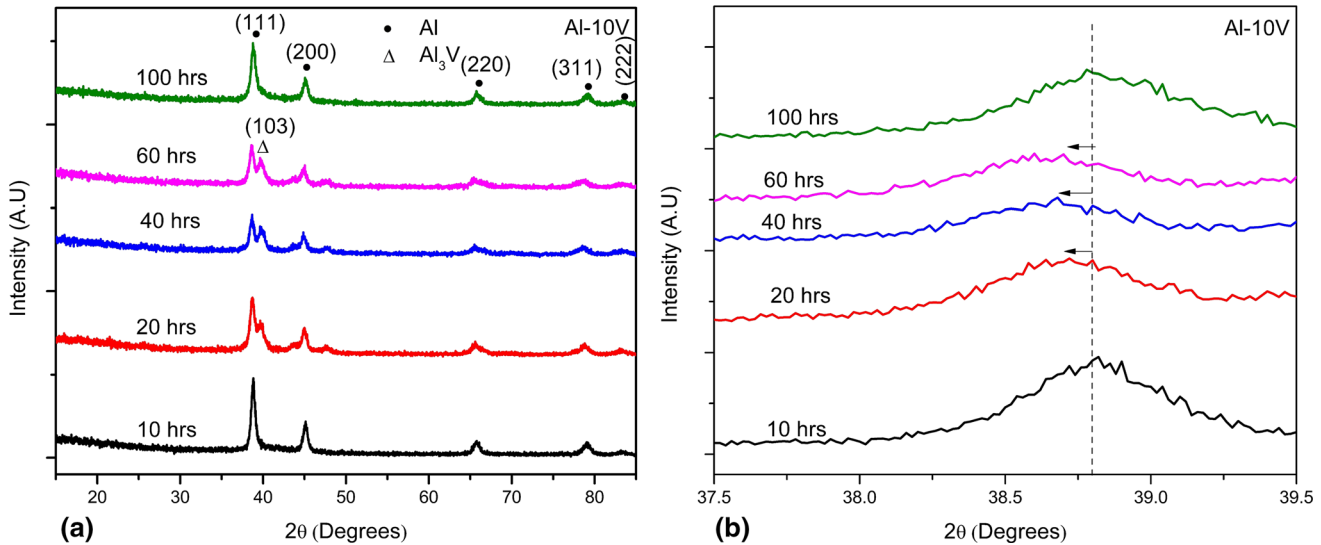


Fig. 12. XRD scans for HEBM Al-10at.%V for different milling times (a) complete XRD scan at 350 RPM, (b) zoomed region at 350 RPM, showing peak shift corresponding to Al (111) for various milling times

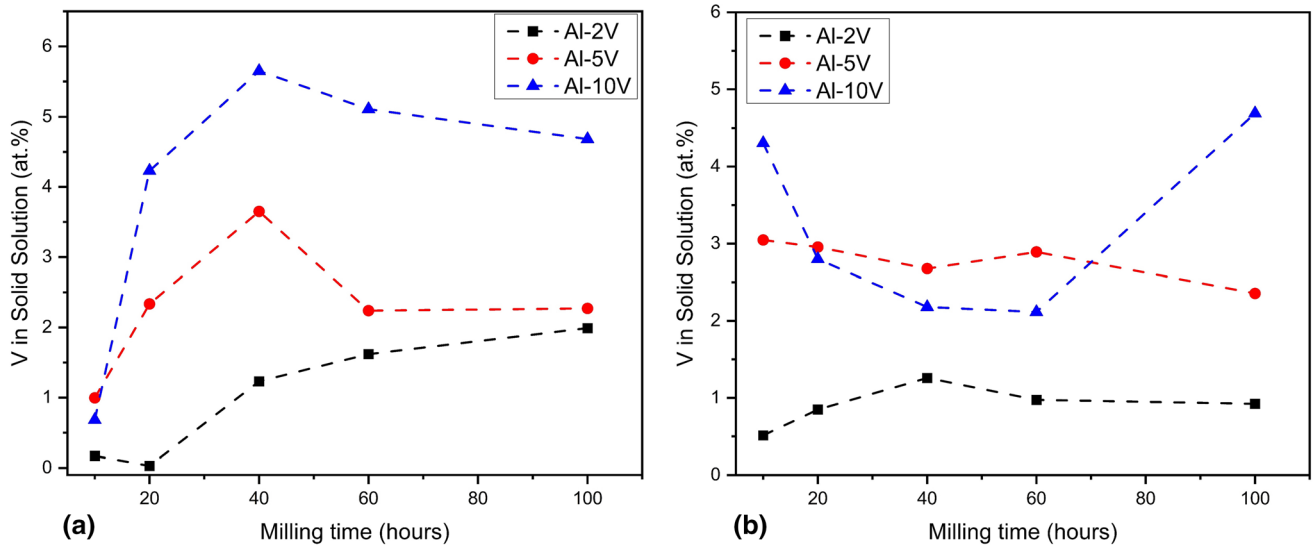


Fig. 13. The amount of alloying element presents in the solid solution in different alloying compositions estimated using XRD analysis, variation with ball milling time, respectively. (a) 280 RPM and (b) 350 RPM

hardness until 60 hours followed by a sharp drop in the last 40 hours of ball milling. In Al-10at%V, a significant reduction in hardness in the first 40 hours was observed, followed by a rapid increment with continuous ball milling. Also, the average grain size did not fluctuate significantly with ball milling time in all the compositions at 350 RPM. Therefore, it can be suggested that the contribution from the grain refinement for hardness fluctuation is insignificant. It can be observed that the solid solubility dropped with ball milling time in Al-10 at.%V at 350 rpm. In consequence, solid solution strengthening reduction can be noticed with ball milling time in Al-10 at.%V at 350 RPM.

The theoretical hardness of HEBM aluminum vanadium alloy can be attributed to the combined influence of the hardness of the pure Al [$\sigma_o \sim 20$ MPa (Ref 1, 3)], solid solution strengthening, grain refinement strengthening, and Orowan strengthening. According to the literature (Ref 1, 50),

the mechanisms of each strengthening contribution can be calculated separately.

1. Solid solution strengthening (σ_{ss}) can be estimated using Eq 2 :

$$\sigma_{ss} = HC^\alpha \quad (\text{Eq 2})$$

Where α and H are constants associated with the alloy properties, and C is the concentration of solute atoms in at.%. For ball-milled Al-xV alloys, α is 1 and H is 68 MPa at.%⁻¹ (Ref 3). The solid solubility that was calculated using XRD was used to estimate the solid solution strength for each composition.

2. Grain boundary strengthening (σ_{gb}) can be estimated using the Eq 3 (Ref 3, 50, 53, 54):

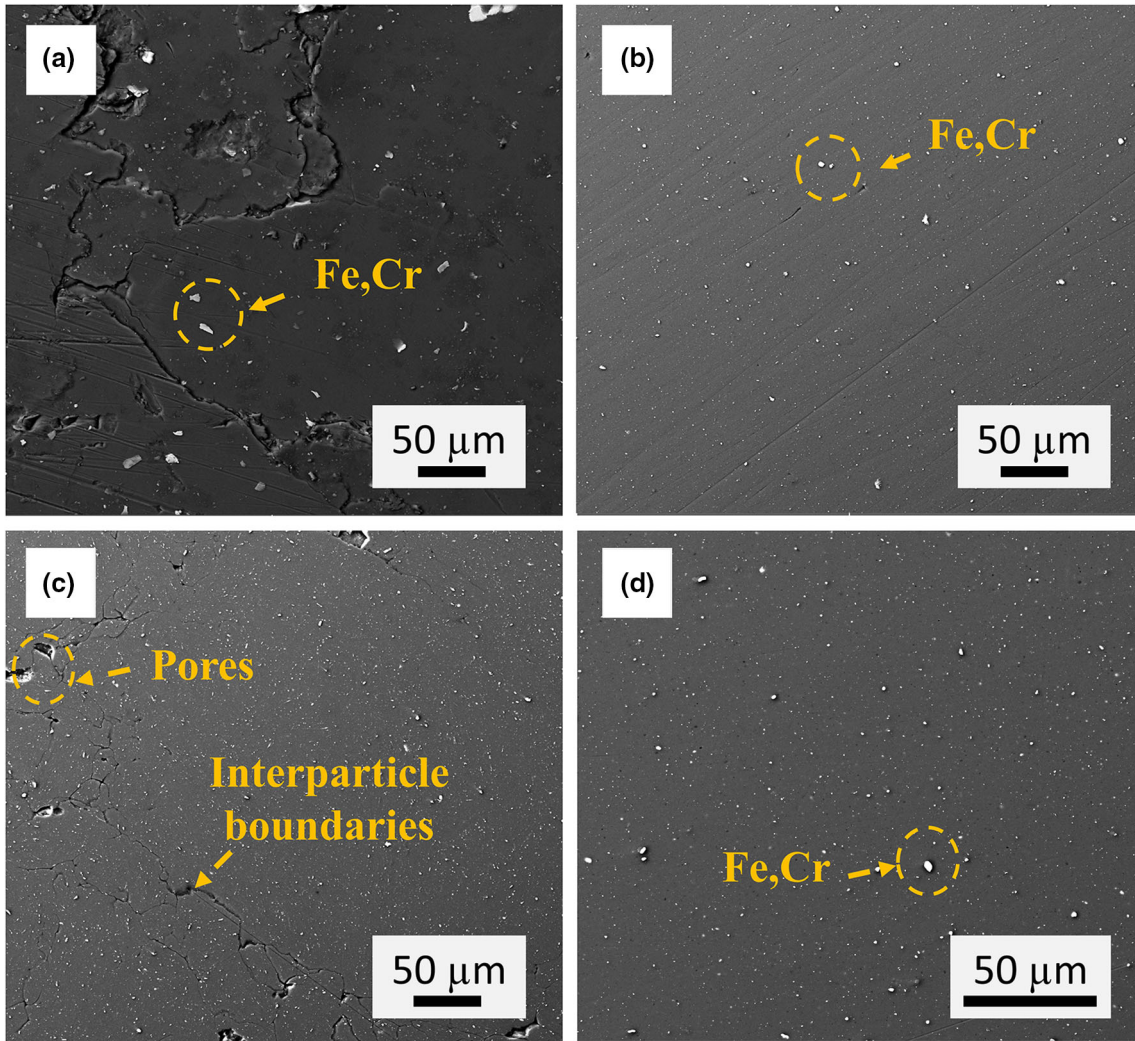


Fig. 14. BSE images of Al-2at.%V alloy for: (a) 10, (b) 100, h of milling at 280 RPM (c) 10, (d) 100 h of HEBM at 350 RPM, and subsequent cold compaction

$$\sigma_{gb} \approx \frac{k}{d^{1/2}} \quad (\text{Eq 3})$$

Where k is a material constant (Hall-Petch coefficient), and d is grain size. For ball-milled Aluminum alloys, k is reported as $0.09 \text{ MPam}^{1/2}$ (Ref 1, 3, 50). The grain size that was estimated using XRD was used to estimate grain boundary strengthening for each composition.

3. The Orowan strengthening (σ_{Or}) extension can be calculated from the Eq 4 (Ref 1, 50):

$$\sigma_{Or} = \sqrt{3} \left[\frac{Gb \ln(d)}{2\pi(d)} \left[\frac{\ln(2r)}{\ln(d)} \right]^{3/2} \right] \quad (\text{Eq 4})$$

Where G is the shear modulus (26 GPa for Al), b is the burger vector (0.286 nm for Al), d is the mean interparticle distance, and r is the mean radius of the particles. However, SEM did not reveal enough information to estimate precipitation size and distribution. The maximum contribution from the Orowan strengthening of Al-x at.%V ($x = 2, 5$ and 10) estimated by the deviation of theoretical strength from experimental yield strength which is around 9%. In comparison, it is reported the contribution of Orowan strengthening in a HEBM Al-20at.%Cr alloy was calculated to be 6.9% of the total strength (Ref 1). Also, a high-resolution technique like TEM is required to estimate the precipitation size and distribution accurately.

The total theoretical strength of ball-milled aluminum alloys can be calculated using Eq 5 (Ref 1, 50):

$$\sigma \approx \sigma_o + \sigma_{ss} + \sigma_{gb} + \sigma_{Or} \quad (\text{Eq 5})$$

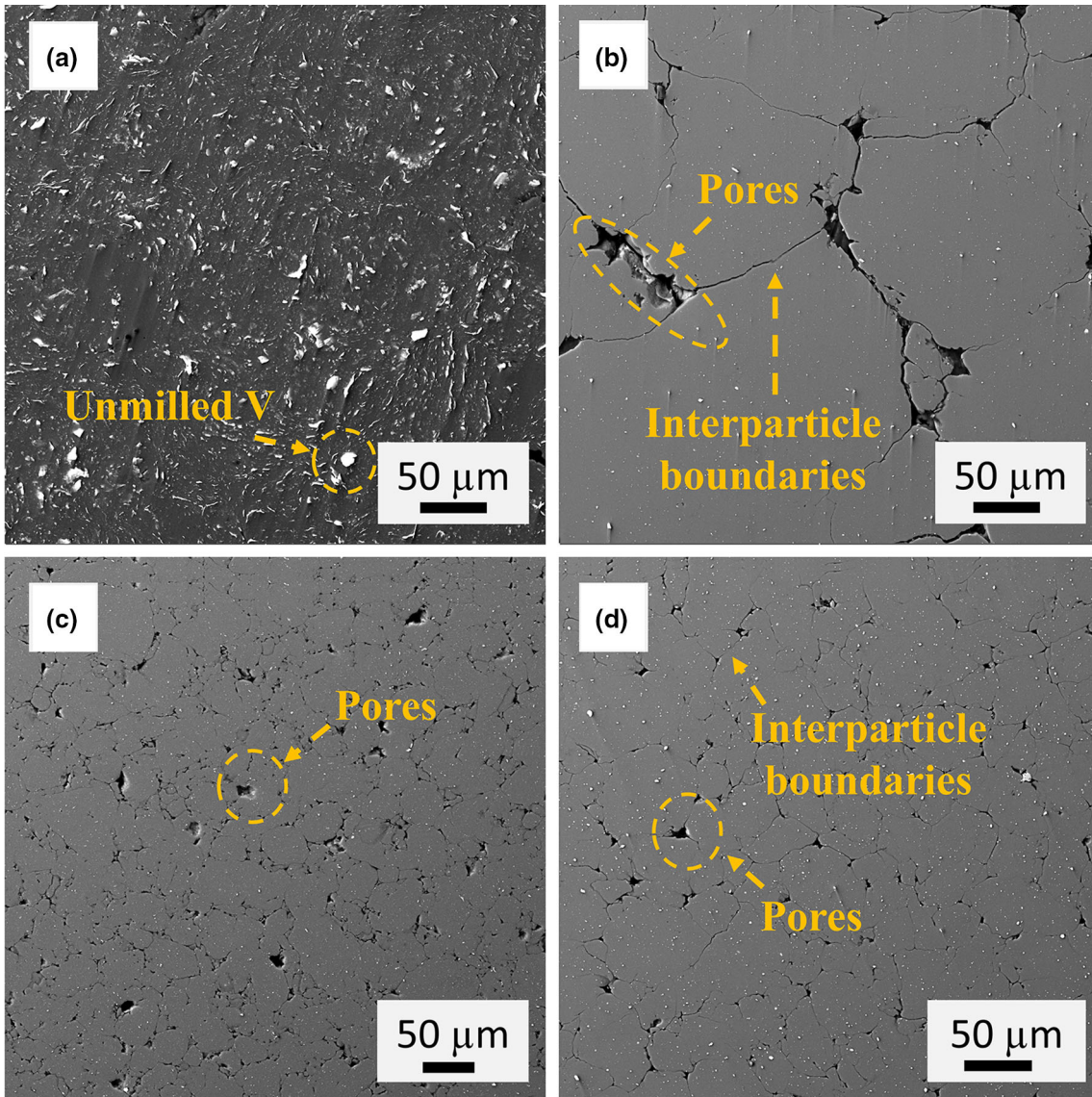


Fig. 15. BSE images of Al-5at.%V alloy for: (a) 10, (b) 100, h of milling at 280 RPM (c) 10, (d) 100 h of HEBM at 350 RPM, and subsequent cold compaction

Figure 19a and b shows the theoretical yield strength ignoring the contribution from Orowan strengthening and is compared with the experimental yield strength obtained using Tabor's rule. It was seen that the experimental yield strengths were approximately equal to the theoretical yield strength in Al-2at.%V, Al-5at.%V and Al-10at.%V at 280 rpm which indicates that the influence from Orowan strengthening is insignificant. Whereas 350 rpm showed a higher experimental yield strength which indicated higher rpm would facilitate some other minor strengthening mechanisms. However, the theoretical grain refinement strengthening is almost 70% of the total theoretical strength for each composition. Hence, it can be suggested that the main strengthening of these alloys is attributed to grain refinement.

The experimental yield strength is plotted as a function of the inverse square root of grain diameter (Fig. 20a and b). The Hall-Petch coefficient was calculated using the slope of the graph and was $0.23 \text{ MPam}^{1/2}$ and $0.12 \text{ MPam}^{1/2}$ for both 280 and 350 rpm, respectively. These estimated Hall-Petch coefficient values were slightly higher than that is reported in the literature (Ref 50, 55, 56). The estimation of the Hall-Petch coefficient was done using the total experimental yield strength. However, the grain refinement strengthening is almost 70% of the total experimental yield strength. Therefore, it is expected to have a higher Hall-Petch coefficient than that is reported in the literature.

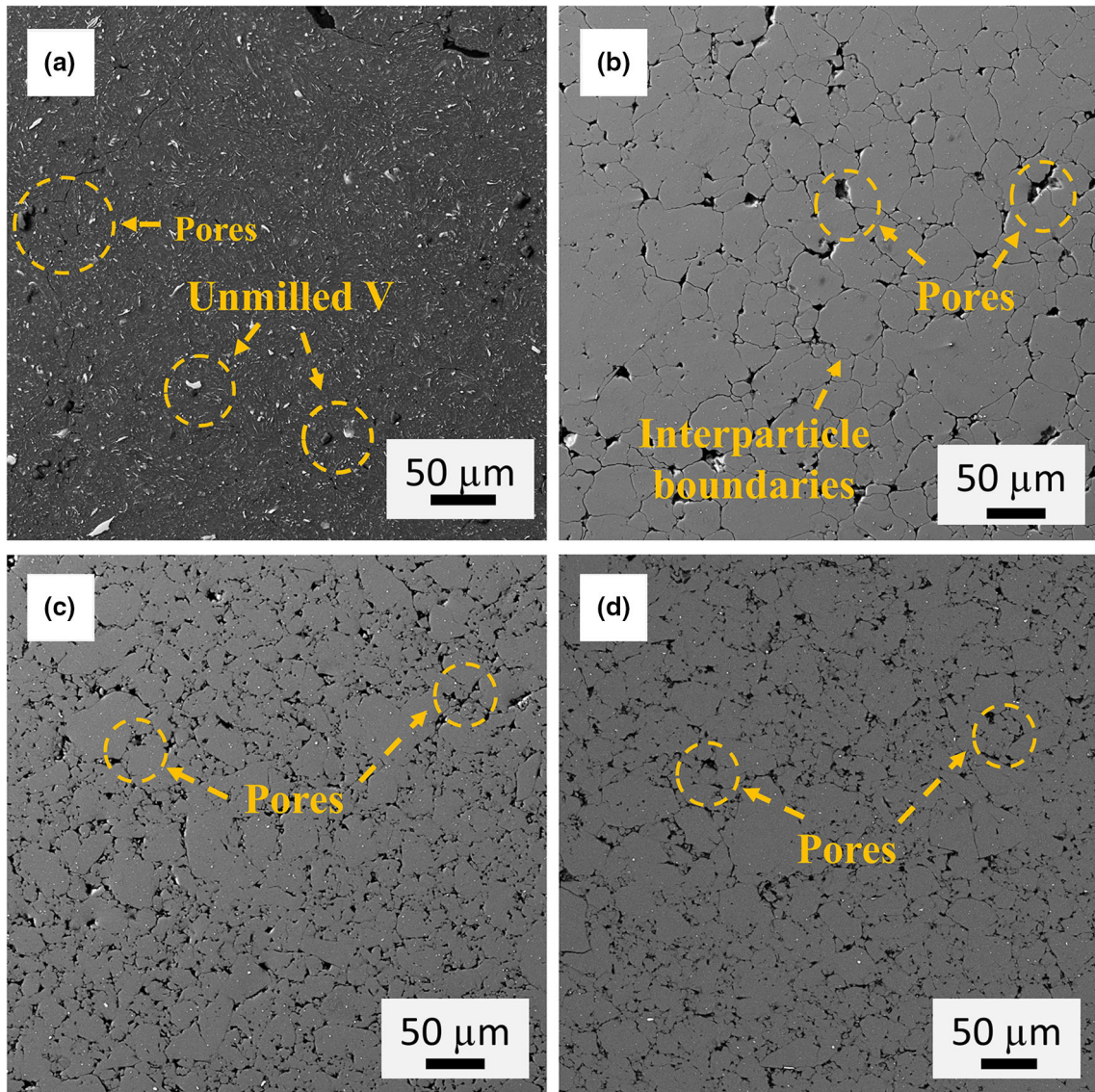


Fig. 16. BSE images of Al-10at.%V alloy for: (a) 10, (b) 100, h of milling at 280 RPM (c) 10, (d) 100 h of HEBM at 350 RPM, and subsequent cold compaction

3.4 Corrosion Behavior

Corrosion behavior was studied using potentiodynamic polarization tests. The typical potentiodynamic polarization curves for Al-xV ($x = 2, 5$ and 10 at.%) after milling 100, 40, and 40 hours at 280 rpm, respectively, are shown in Fig. 21. The passive current density was less than $\sim 1\mu\text{A}/\text{cm}^2$ in all three compositions. The pitting potential was increased with the V addition and was $\sim (-427.12 \pm 5.65)\text{mV}_{\text{SCE}}$ for Al-2at.%V which is less noble than that in Al-5at.%V and Al-10at.%V ($\sim (-190.24 \pm 5.61)\text{mV}_{\text{SCE}}, (-167.08 \pm 3.89)\text{mV}_{\text{SCE}}$,

respectively). The V addition can be attributed to the passive film enrichment which could cause an improvement of the pitting potentials in these alloys. The repassivation tendency, as measured by repassivation potential, was also increased with V content indicated that the V addition could reduce the dissolution of the alloy which may interrupt the formation of the critical pit solution. A similar corrosion resistance improvement in several Al alloy systems is reported in the literature which is further supported that the corrosion resistance is attributed to the addition of V, extended solid solution, and the nanostructure (Ref 26, 57). It should be noted that pitting

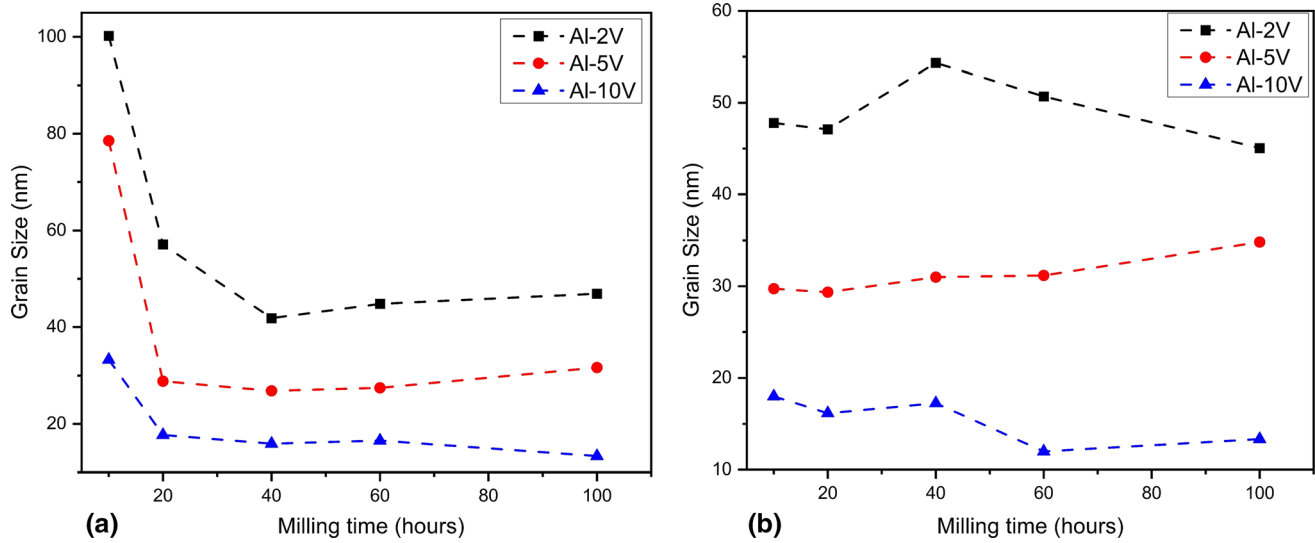


Fig. 17. The grain size of HEBM alloys variation with ball milling time for different alloying compositions: (a) 280 RPM and (b) 350 RPM

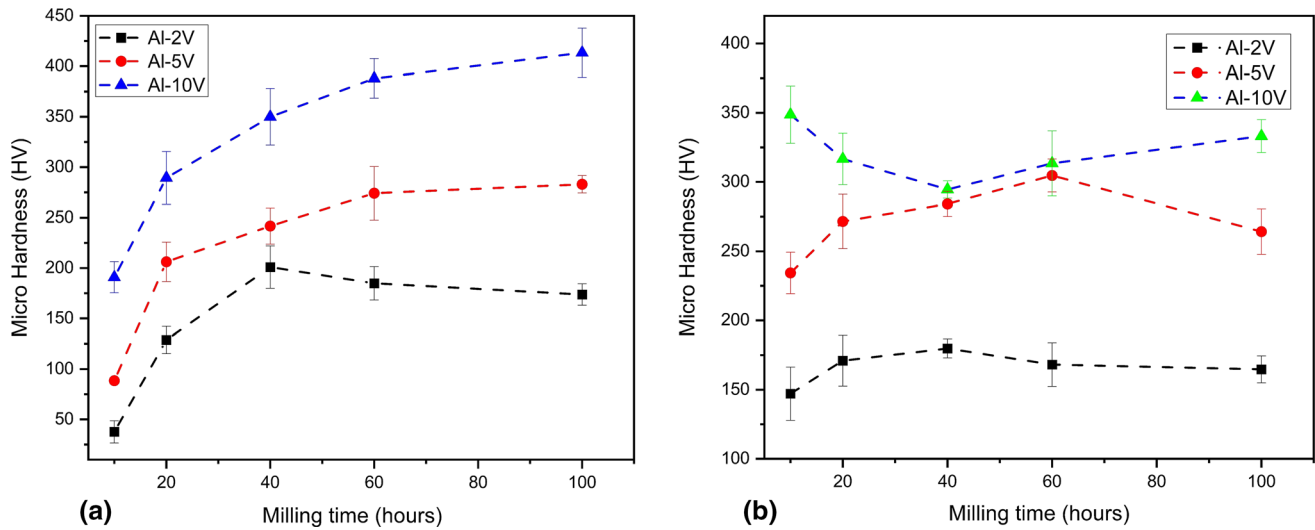


Fig. 18. Vickers microhardness of HEBM alloys as a function of ball milling time in different alloying (a) 280 RPM and (b) 350 RPM

corrosion resistance, as reported by the pitting potential, is significantly higher than the commercial alloys and is in good agreement with the proposed increase in corrosion resistance in the ball milling alloys (Ref 1, 2, 25, 26, 49).

4. Conclusions

In this study, the influence of HEBM time and speed on the grain size, solid solubility, and hardness was investigated. The key findings are as follows:

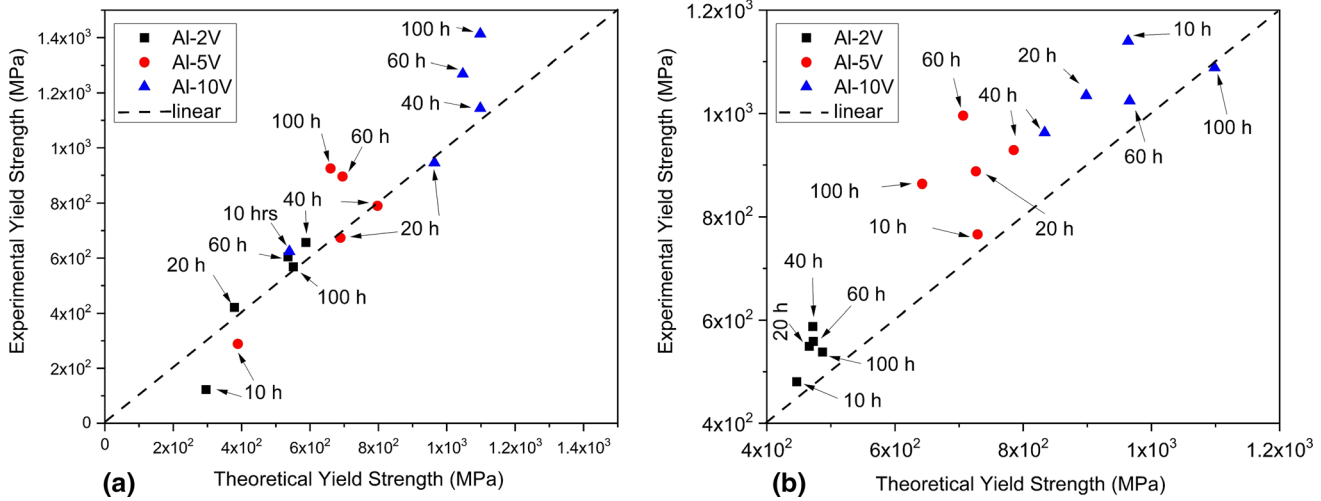


Fig. 19. Experimental yield strength extrapolated by hardness and theoretical yield strength calculated by Eq 5 for different milling times of HEBM alloys (a) 280 rpm and (b) 350 rpm

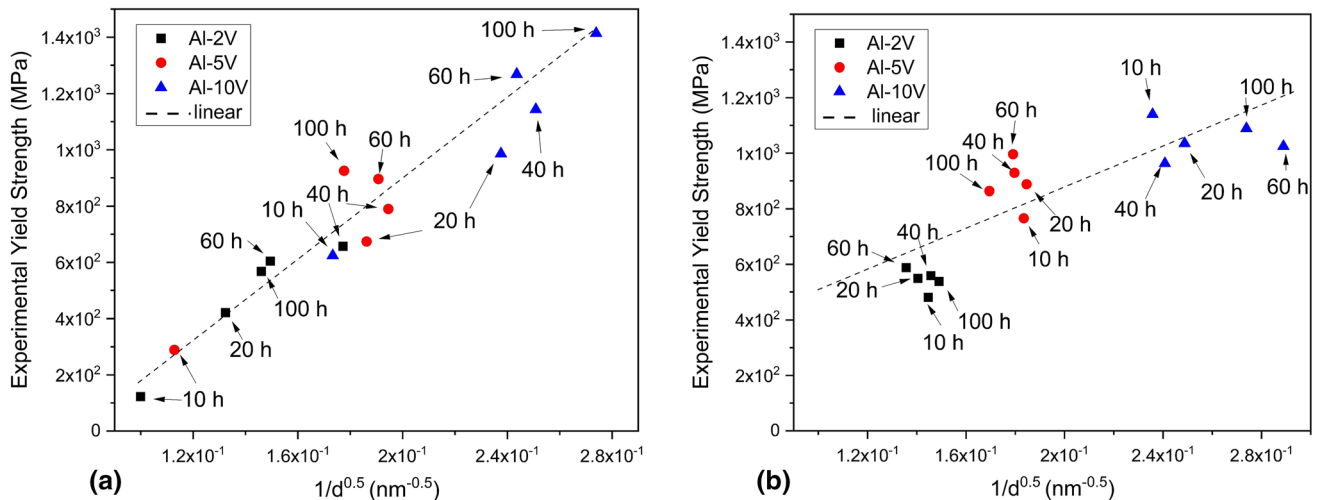


Fig. 20. Experimental yield strength extrapolated by hardness and the reciprocal square root of the grain diameter for different milling times of HEBM alloys (a) 280 rpm and (b) 350 rpm

- The solid solubility of V for the three alloys Al-xV ($x = 2, 5$, and 10 at.%) was influenced by the ball milling time and speed. At the milling speed of 280 RPM, solid solubility of V for Al-2at.%V increased with ball milling time while for Al-5 at.%V and Al-10 at.%V highest solid solubility was achieved after 40 hours of ball milling for both compositions. Milling at 350 RPM decreased the time required to achieve the highest solid solubility. However, the highest achievable solid solubility for the three alloys was higher for milling at 280 RPM.
- The grain size of the alloys showed a strong dependency on the milling time, milling speed, and V content. The

grain size of all the alloys was below 100 nm after 10 hours of milling. The rate of the grain refinement was dependent upon the milling speed, while the minimum achievable grain size showed a strong dependency on the V content.

- The solid solubility, grain refinement, and hardness improved significantly with V content. The highest solid solubility, grain refinement, and hardness were observed in Al-10 at.%V at 280 RPM.
- The corrosion resistance improved with V content and the highest pitting potential was appeared in Al-10 at.%V produced by milling at 280 RPM.

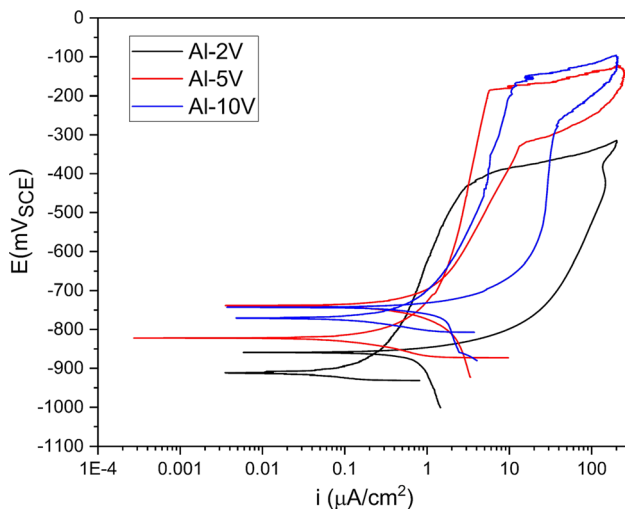


Fig. 21. Representative potentiodynamic polarization curves for Al-xV (x=2,5 and 10 at.%) for optimized milling times (100, 40, and 40 hours of ball milling, respectively) at selected speed (280 rpm). The tests were conducted in 0.01M NaCl after 30 minutes of stabilization of open circuit potential

Acknowledgment

The financial support from the National Science Foundation (NSF-CMMI 1760204) under the supervision of Dr. Alexis Lewis is greatly acknowledged. The authors would like to acknowledge the Department of Chemical, Biomolecular and Corrosion Engineering and National Polymer Innovation Center (NPIC), the University of Akron for the SEM, XRD, and hardness tests.

References

- R.K. Gupta, D. Fabijanic and T. Dorin, Simultaneous Improvement in the Strength and Corrosion Resistance of Al Via High-Energy Ball Milling and Cr Alloying, *Mater. Des.*, 2015, **84**, p 270–276. <https://doi.org/10.1016/J.MATDES.2015.06.120>
- J. Esquivel, H.A. Murdoch, K.A. Darling and R.K. Gupta, Excellent Corrosion Resistance and Hardness in Al Alloys by Extended Solid Solubility and Nanocrystalline Structure, *Mater. Res. Lett.*, 2018, **6**(1), p 79–83. <https://doi.org/10.1080/21663831.2017.1396262>
- J. Esquivel and R.K. Gupta, Influence of the V Content on Microstructure and Hardness of High-Energy Ball Milled Nanocrystalline Al-V Alloys, *J. Alloys Compd.*, 2018, **760**, p 63–70. <https://doi.org/10.1016/J.JALLOCOM.2018.05.132>
- K. Lu, Materials Science. The Future of Metals, *Mater. Sci.*, 2010, **4**(2), 126, doi: <https://doi.org/10.1126/science.1182769>
- P.M. Natishan, E. McCafferty and G.K. Hubler, The Corrosion Behavior of Mo-Al, Cr-Al and Cr-Mo-Al Surface Alloys Produced by Ion Beam Mixing and Ion Implantation, *Corros. Sci.*, 1991, **32**(7), p 721–731. [https://doi.org/10.1016/0010-938X\(91\)90086-5](https://doi.org/10.1016/0010-938X(91)90086-5)
- R.K. Gupta, B.S. Murty and N. Birbilis, *An Overview of High-Energy Ball Milled Nanocrystalline Aluminum Alloys*, Springer International Publishing, Cham, 2017
- S.M.A. Shibli, S.R. Archana and P. Muhamed Ashraf, Development of Nano Cerium Oxide Incorporated Aluminium Alloy Sacrificial Anode for Marine Applications, *Corros. Sci.*, 2008, **50**(8), p 2232–2238. <https://doi.org/10.1016/j.corsci.2008.06.017>
- B. Zhang, W. Xu, Q. Zhu, Y. Sun and Y. Li, Mechanically robust superhydrophobic porous anodized AA5083 for marine corrosion protection, *Corros. Sci.*, 2019, **158**, p 108083. <https://doi.org/10.1016/j.corsci.2019.06.031>
- P. Rambabu, N. Eswara Prasad, V. V. Kutumbarao, and R. J. H. Wanhill, “*Aluminium Alloys for Aerospace Applications*,” Springer, Singapore, 2017, pp. 29–52
- R.C. Dorward and T.R. Pritchett, Advanced Aluminium Alloys for Aircraft and Aerospace Applications, *Mater. Des.*, 1988, **9**(2), p 63–69. [https://doi.org/10.1016/0261-3069\(88\)90076-3](https://doi.org/10.1016/0261-3069(88)90076-3)
- G. Sakai, Z. Horita and T.G. Langdon, Grain Refinement and Superplasticity in an Aluminum Alloy Processed by High-Pressure Torsion, *Mater. Sci. Eng. A*, 2005, **393**(1–2), p 344–351. <https://doi.org/10.1016/j.msea.2004.11.007>
- M.Y. Murashkin, A.R. Kil'Mametov and R.Z. Valiev, Structure and Mechanical Properties of an Aluminum ALLOY 1570 Subjected to Severe Plastic Deformation by High-Pressure Torsion, *Phys. Met. Metallogr.*, 2008, **106**(1), p 90–96. <https://doi.org/10.1134/S0031918X08070120>
- W.C. Moshier, Surface Chemistry of Sputter-Deposited Al-Mo and Al-Cr Alloys Polarized in 0.1N KCl, *J. Electrochem. Soc.*, 1989, **136**(2), p 356. <https://doi.org/10.1149/1.2096635>
- H. Yoshioka, Q. Yan and H. Habazaki, Passivity and its Breakdown on Sputter-Deposited Amorphous Al-Early Transition Metal Alloys in 1 M HCl at 30°C, *Corros. Sci.*, 1990, **31**, p 349–354. [https://doi.org/10.1016/0010-938X\(90\)90130-W](https://doi.org/10.1016/0010-938X(90)90130-W)
- E. Akiyama, A. Kawashima and K. Asami, The Effects of Alloying Elements on the Passivity of Sputter-Deposited Amorphous Al-Cr-Mo Alloys in 1 M HCl, *Corros. Sci.*, 1996, **38**(8), p 1281–1294. [https://doi.org/10.1016/0010-938X\(96\)00017-0](https://doi.org/10.1016/0010-938X(96)00017-0)
- H. Yoshioka, H. Habazaki and A. Kawashima, An XPS Study of the Corrosion Behavior of Sputter-Deposited Amorphous Al-W Alloys in 1 M HCl, *Corros. Sci.*, 1991, **32**(3), p 313–325. [https://doi.org/10.1016/0010-938X\(91\)90076-2](https://doi.org/10.1016/0010-938X(91)90076-2)
- G.D. Davis, Evolution of the Chemistry of Passive Films of Sputter-Deposited, Supersaturated Al Alloys, *J. Electrochem. Soc.*, 1990, **137**(2), p 422. <https://doi.org/10.1149/1.2086456>
- T. Tsuda and C.L. Hussey, Electrochemistry of Vanadium(II) and the Electrodeposition of Aluminum-Vanadium Alloys in the Aluminum Chloride-1-Ethyl-3-Methylimidazolium Chloride Molten Salt, *J. Min. Metall. Sect. B Metall.*, 2003, **39**(1–2), p 3–22. <https://doi.org/10.2298/jmmb0302003t>
- T.P. Moffat, Pitting Corrosion of Electrodeposited Aluminum-Manganese Alloys, *J. Electrochem. Soc.*, 1993, **140**(10), p 2779–2786. <https://doi.org/10.1149/1.2220910>
- S. Venkatraman, M.R. Nair and D.C. Kothari, Anodic Polarization Behaviour of Ion Implanted Aluminum in 3.5 wt.% NaCl Electrolyte, *Nucl. Inst. Methods Phys. Res. B*, 1987, **19–20**, p 241–246. [https://doi.org/10.1016/S0168-583X\(87\)80051-4](https://doi.org/10.1016/S0168-583X(87)80051-4)
- M.V. Zeller and J.A. Kargol, Surface Analysis Studies on the Corrosion Resistance of Mo Implanted Al Alloys, *Appl. Surf. Sci.*, 1984, **18**(1–2), p 63–85. [https://doi.org/10.1016/0378-5963\(84\)90038-2](https://doi.org/10.1016/0378-5963(84)90038-2)
- P.M. Natishan, E. McCafferty and G.K. Hubler, Localized Corrosion Behavior of Aluminum Surface Alloys Produced by Ion Implantation and ION BEAM MIXING, *Mater. Sci. Eng. A*, 1989, **116**, p 41–46. [https://doi.org/10.1016/0921-5093\(89\)90125-1](https://doi.org/10.1016/0921-5093(89)90125-1)
- V. Ashworth, W.A. Grant and R.P.M. Procter, Novel Corrosion Resistant Alloys by Ion Implantation, *Ind. Eng. Chem. Prod. Res. Dev.*, 1978, **17**(2), p 176–182. <https://doi.org/10.1021/i360066a018>
- D.L. Zhang, Processing of advanced materials using high-energy mechanical milling, *Prog. Mater. Sci.*, 2004, **49**(3–4), p 537–560. [https://doi.org/10.1016/S0079-6425\(03\)00034-3](https://doi.org/10.1016/S0079-6425(03)00034-3)
- J. Esquivel and R.K. Gupta, Corrosion Behavior and Hardness of Al-M (M: Mo, Si, Ti, Cr) Alloys, *Acta Metall. Sin. English Lett.*, 2017, **30**(4), p 333–341. <https://doi.org/10.1007/s40195-017-0550-2>
- R.K. Gupta, D. Fabijanic, R. Zhang and N. Birbilis, Corrosion Behaviour and Hardness of In Situ Consolidated Nanostructured Al and Al-Cr Alloys Produced Via High-Energy Ball Milling, *Corros. Sci.*, 2015, **98**, p 643–650. <https://doi.org/10.1016/j.corsci.2015.06.011>
- J. Esquivel, M.G. Wachowiak, S.P. O'Brien and R.K. Gupta, Thermal Stability of Nanocrystalline Al-5at.%Ni and Al-5at.%V Alloys Produced by High-Energy Ball Milling, *J. Alloys Compd.*, 2018, **744**, p 651–657. <https://doi.org/10.1016/j.jallcom.2018.02.144>
- C. Suryanarayana, E. Ivanov and V.V. Boldyrev, The Science and Technology of Mechanical Alloying, *Mater. Sci. Eng. A*, 2001, **304**(1–2), p 151–158. [https://doi.org/10.1016/S0921-5093\(00\)01465-9](https://doi.org/10.1016/S0921-5093(00)01465-9)
- C. Suryanarayana, Mechanical Alloying and Milling, *Prog. Mater. Sci.*, 2001, **46**(1–2), p 1–184. [https://doi.org/10.1016/S0079-6425\(99\)00010-9](https://doi.org/10.1016/S0079-6425(99)00010-9)
- C. Suryanarayana, Phase Formation Under Non-equilibrium Processing Conditions: Rapid Solidification Processing and Mechanical Alloying,

J. Mater. Sci., 2018, **53**(19), p 13364–13379. <https://doi.org/10.1007/s10853-018-2197-4>

31. J. Lv, W. Guo, T. Liang and M. Yang, The Effects of Ball Milling Time and Surface Enriched Chromium on Microstructures and Corrosion Resistance of AISI 304 Stainless Steel, *Mater. Chem. Phys.*, 2017, **197**, p 79–86. <https://doi.org/10.1016/j.matchemphys.2017.05.026>

32. X. Zhou, R. Wang, C. Li, X. Wang, K. Wang and Q. Wang, Effect of High-Energy Ball Milling on the Microstructure and Properties of Ultrafine Gradient Cemented Carbides, *Int. J. Appl. Ceram. Technol.*, 2020, **17**(5), p 2298–2306. <https://doi.org/10.1111/ijac.13551>

33. M. Ravithul Basariya, V. C. Srivastava, and N. K. Mukhopadhyay, Effect of Milling Time on Structural Evolution and Mechanical Properties of Garnet Reinforced EN AW6082 Composites, *Mettal. Mater. Trans. A Phys. Metall. Mater. Sci.*, 2015, **46**(3), 1360–1373, doi: <https://doi.org/10.1007/s11661-014-2685-3>

34. J. Feng, H.-F. Sun and W.-B. Fang, Effect of Ball Milling Time on Nanocrystalline Powders and Bulk Ultrafine-Grained Mg-3Al-Zn Alloy, *MATEC Web Conf.*, 2015, **21**, p 11006. <https://doi.org/10.1051/matecconf/20152111006>

35. E. Saker, N. Loudjani, M. Benchiheub and M. Bououdina, Influence of Milling Time on Structural and Microstructural Parameters of Ni50Ti50 Prepared by Mechanical Alloying Using Rietveld Analysis, *J. Nanomater.*, 2018 <https://doi.org/10.1155/2018/2560641>

36. L. Esteves et al., Corrosion Behavior of AA5083 Produced by High-Energy Ball Milling, *J. Alloys Compd.*, 2021, **857**, p 158268. <https://doi.org/10.1016/j.jallcom.2020.158268>

37. B.D. Cullity and S.R. Stock, *Element of X-Ray Diffraction, 3rd Edition*, Pearson Education Limited, London, 2014

38. A. L. Patterson, The Scherrer Formula for x-Ray Particle Size Determination, *Phys. Rev.*, 1939, **56**, 978–982, Accessed 06 June 2019. [Online]. <https://journals.aps.org/pr/pdf/https://doi.org/10.1103/PhysRev.56.978>

39. J.S. Williams and W.A. Grant, The Application of High Resolution Rutherford Backscattering to the Measurement of Ion Ranges in Si and Al, *Radiat. Eff.*, 1975, **25**(1), p 55–56. <https://doi.org/10.1080/00337577508242056>

40. A. Valério and S. L. Morelhão, Usage of Scherrer's Formula in X-ray Diffraction Analysis of Size Distribution in Systems of Monocrystalline Nanoparticles, *Condens. Mater. Sci.*, 2019

41. T. Uesugi and K. Higashi, First-Principles Studies on Lattice Constants and Local Lattice Distortions in Solid Solution Aluminum Alloys, *Comput. Mater. Sci.*, 2013, **67**, p 1–10. <https://doi.org/10.1016/j.commat.2012.08.037>

42. O. Seo, J. Kim and S. Hiroi, Lattice Constant, Bond-Orientational Order, and Solid Solubility of PdPt Bimetallic Nanoparticles, *Appl. Phys. Lett.*, 2018, **113**, p 71907. <https://doi.org/10.1063/1.5040661>

43. K. Sikdar, S. Chakravarty and D. Roy, Synthesis and Characterization of an In Situ Consolidated Nanocrystalline Cu88Al11.5Y0.5 Alloy, *J. Alloys Compd.*, 2017, **717**, p 219–225. <https://doi.org/10.1016/j.jallcom.2017.05.092>

44. S. Cheng, E. Ma, Y.M. Wang and L.J. Kecske, Tensile Properties of In Situ Consolidated Nanocrystalline Cu, *Acta Mater.*, 2005, **53**(5), p 1521–1533. <https://doi.org/10.1016/j.actamat.2004.12.005>

45. R.K. Gupta, K.S. Darling and R.K. Sing Raman, Synthesis, characterization And Mechanical Behaviour of an in Situ Consolidated Nanocrystalline FeCrNi Alloy, *J. Mater. Sci.*, 2012, **47**(3), p 1562–1566. <https://doi.org/10.1007/s10853-011-5986-6>

46. L. Zhang et al., Effects of Mechanical Ball Milling Time on the Microstructure and Mechanical Properties of Mo2NiB2-Ni Cermets, *Materials (Basel)*, 2019, **12**(12), p 1926. <https://doi.org/10.3390/ma12121926>

47. J. Xu, G.S. Collins, L.S.J. Peng and M. Atzman, Deformation-Assisted Decomposition of Unstable Fe50Cu50 Solid Solution During Low-Energy Ball Milling, *Acta Mater.*, 1999, **47**(4), p 1241–1253. [https://doi.org/10.1016/S1359-6454\(98\)00428-5](https://doi.org/10.1016/S1359-6454(98)00428-5)

48. Y. Luo, G. Ran, N. Chen, Q. Shen and Y. Zhang, Microstructural Evolution, Thermodynamics, and Kinetics of Mo-Tm2O3 Powder Mixtures During Ball Milling, *Materials (Basel)*, 2016 <https://doi.org/10.3390/ma9100834>

49. R.K. Gupta, A. Deschamps and M.K. Cavanaugh, Relating the Early Evolution of Microstructure with the Electrochemical Response and Mechanical Performance of a Cu-Rich and Cu-Lean 7xxx Aluminum Alloy, *J. Electrochem. Soc.*, 2012, **159**(11), p 492–502. <https://doi.org/10.1149/2.062211jes>

50. K.A. Darling, A.J. Roberts and L. Armstrong, Influence of Mn Solute Content on Grain Size Reduction and Improved Strength in Mechanically Alloyed Al-Mn Alloys, *Mater. Sci. Eng. A*, 2014, **589**, p 57–65. <https://doi.org/10.1016/j.msea.2013.09.047>

51. K.D. Ralston, N. Birbilis and M. Weyland, The Effect of Precipitate Size on the Yield Strength-Pitting Corrosion Correlation in Al-Cu-Mg Alloys, *Acta Mater.*, 2010, **58**(18), p 5941–5948. <https://doi.org/10.1016/j.actamat.2010.07.010>

52. Z. Wu, Y. Liang and E. Fu, Effect of Ball Milling Parameters on the Refinement of Tungsten Powder, *Metals (Basel)*, 2018, **8**(4), p 281–295. <https://doi.org/10.3390/met8040281>

53. N. Naga Krishna, R. Tejas, K. Sivaprasad and K. Venkateswarlu, Study on Cryorolled Al-Cu Alloy Using X-ray Diffraction Line Profile Analysis and Evaluation Of Strengthening Mechanisms, *Mater. Des.*, 2013, **52**, p 785–790. <https://doi.org/10.1016/j.matedes.2013.05.095>

54. T. Shanmugasundaram, M. Heilmair, B.S. Murty and V.S. Sarma, On the Hall-Petch Relationship in a Nanostructured Al-Cu Alloy, *Mater. Sci. Eng. A*, 2010, **527**(29–30), p 7821–7825. <https://doi.org/10.1016/j.msea.2010.08.070>

55. H. Hasegawa et al., Thermal Stability of Ultrafine-Grained Aluminum in the Presence of Mg and Zr Additions, *Mater. Sci. Eng. A*, 1999, **265**(1–2), p 188–196. [https://doi.org/10.1016/s0921-5093\(98\)01136-8](https://doi.org/10.1016/s0921-5093(98)01136-8)

56. D.B. Witkin and E.J. Lavernia, Synthesis and Mechanical Behavior of Nanostructured Materials Via Cryomilling, *Prog. Mater. Sci.*, 2006, **51**(1), p 1–60. <https://doi.org/10.1016/j.pmatsci.2005.04.004>

57. L. Liu, Y. Li, and F. Wang, Electrochemical Corrosion Behavior of Nanocrystalline Materials: A Review, *J. Mater. Sci. Technol.*, 2010, **26**(1), 1–14. (Chinese Society of Metals). doi: [https://doi.org/10.1016/S1005-0302\(10\)60001-1](https://doi.org/10.1016/S1005-0302(10)60001-1)

58. Y.S. Kwon, P.P. Choi, J.S. Kim, D.H. Kwon and K.B. Gerasimov, Decomposition of Intermetallics During High-Energy Ball-Milling, *Mater. Sci. Eng. A*, 2007, **449**, p 1083–1086. <https://doi.org/10.1016/j.msea.2006.02.267>

Publisher's Note Springer Nature remains neutral with regard to jurisdictional claims in published maps and institutional affiliations.